Atmospheric Research 294 (2023) 106975

Contents lists available at ScienceDirect

Atmospheric Research

journal homepage: www.elsevier.com/locate/atmosres

Evaluating the climate projections for China through the lens of the simulations of planetary boundary layer height

Junlei Meng [a], Yang Gao [b,*], Yuhang Wang [c,*], Lifang Sheng [a], Shaoqing Zhang [d]

[a] College of Oceanic and Atmospheric Sciences, Ocean University of China, Qingdao 266100, China
[b] Frontiers Science Center for Deep Ocean Multispheres and Earth System, Key Laboratory of Marine Environmental Science and Ecology, Ministry of Education, Ocean University of China, and Laoshan Laboratory, Qingdao 266100, China
[c] School of Earth and Atmospheric Sciences, Georgia Institute of Technology, Atlanta, GA 30332, USA
[d] Frontiers Science Center for Deep Ocean Multispheres and Earth System, Key Laboratory of Physical Oceanography, Ministry of Education, the College of Oceanic and Atmospheric Sciences, Ocean University of China, and Laoshan Laboratory, Qingdao 266100, China

ARTICLE INFO

Keywords:
Planetary boundary layer height
Climate change
CMIP6 models
Shared socioeconomic pathways
Sensible heat flux

ABSTRACT

The planetary boundary layer height (PBLH) plays an essential role in affecting many meteorological parameters in climate change, and it is closely associated with the concentration of near surface air pollutants as well. Uncertainty of simulating PBLH is large partly due to the complexity in the modulation of surface energy, and the behaviors of the climate models in reproducing PBLH have not been fully evaluated, which also limits the understanding of future changes in PBLH. Here by utilizing a multi-model ensemble of Coupled Model Intercomparison Project Phase 6 (CMIP6), we first thoroughly evaluate the capability of CMIP6 models in reproducing the spatial distribution of PBLH over China during the period of 1995–2014, revealing large discrepancies among the CMIP6 models. Meanwhile, inaccuracy of simulated meteorological parameters can lead to large deviations of PBLH in models, among which sensible heat flux (SHFLX) and near surface relative humidity (RH) show stronger modulation effects. To enhance the confidence of future projections, we apply a method by selecting the five models with the smallest biases and a high signal-to-noise ratio, and the results indicate that changes in PBLH under shared socioeconomic pathways exhibit a dipole pattern in both summer and winter. Specifically, PBLH is projected to decrease over North China and increase over Central China and South China in summer, while in winter PBLH tends to increase stronger in southern China and weaker in the northern flank. To reveal the mechanism governing the PBLH, we find that changes of PBLH is closely associated with surface energy. SHFLX and near surface RH are the dominant factors shaping the changes in the spatial heterogeneity of PBLH in the future. This study has important implications for the improvement of surface energy and PBLH in climate models in order to effectively predict the future changes of air pollutants.

1. Introduction

As an essential part of the atmosphere on Earth, the planetary boundary layer (PBL) affects the vertical exchange of many substances between surface and free atmosphere, including heat, humidity, momentum and air pollutants (Garratt, 1994; von Engeln and Teixeira, 2013). The PBL height (PBLH) is an important parameter representing the characteristics of PBL (Seidel et al., 2010; Zhang et al., 2013), and the development of PBLH is mainly driven by large scale weather conditions and the transport of energy between land and atmosphere, including both latent heat flux and sensible heat flux (Garratt, 1994). PBLH has been widely used to investigate the effects of PBL on air quality (Davy and Esau, 2016; Li et al., 2017), and accurate PBLH simulations are helpful for understanding its influence on air pollutants.

The global climate models (GCMs) are the primary tools used to investigate the PBLH evolutions under a changing climate in future (Fan et al., 2020; Stocker et al., 2013). The PBL process is one of the most important physical processes for numerical models, therefore the inaccuracy of simulated PBLH often leads to weakened meteorological simulation capabilities (Dang et al., 2022; Davy, 2018; Stull, 2006; Vignon et al., 2018). For instance, during the historical period of 1979–2019, CMIP6 models in general capture the spatial heterogeneity globally in the climatological mean and the trend change of PBLH, however, the trend changes in some areas between Coupled Model

* Corresponding authors.
E-mail addresses: yanggao@ouc.edu.cn (Y. Gao), yuhang.wang@eas.gatech.edu (Y. Wang).

https://doi.org/10.1016/j.atmosres.2023.106975
Received 5 April 2023; Received in revised form 5 June 2023; Accepted 23 August 2023
Available online 25 August 2023

Intercomparison Project Phase 6 (CMIP6) and observations may be opposite particularly over the majority of China, and the climatological mean PBLH in CMIP6 is higher than observations (Zhou et al., 2021). A similar finding is shown in a different study (Yue et al., 2021) using CMIP6 ensemble, which focused only on the areas of China, and the opposite signs of PBLH interannual variability between CMIP6 and the reanalysis data ERA5 are largely driven by the opposite variational trends of sensible heat flux between them. Despite large bias in most CMIP6 models, a few models show values close to ERA5, indicating apparent model discrepancies in PBLH simulations. Diagnozing the relationships between PBLH and key meteorological drivers are of great importance to understand the capability of climate models in reproducing the PBLH.

Considering the importance of PBLH on air quality (Petaja et al., 2016; Su et al., 2018), the future change of PBLH is vital of modulating the air pollutant concentrations. Driven by global earth system model CESM, Dou et al. (2021) conducted dynamical downscaling by WRF-Chem, and found decreases of PBLH in mid-century (2031–2050) in northern China under both Representative Concentration Pathway (RCP) 8.5 and RCP 4.5 scenarios. Moreover, there are clear dipole changes in summer demarcated by a line meandering the province borders along with 32°–38°N, exhibiting decrease in northern China and increase across the broad region over Yangtze River Delta (YRD) and the surrounding areas. In contrast, another study of Gao et al. (2019) applied similarly dynamical downscaling method, yielding a contradictory finding with a dominant decrease over the majority of YRD in the mid-century under RCP 4.5, indicating challenges in the robustness of the finding based on a single regional model. Although high-resolution regional climate models are conducted through dynamical downscaling, the biases inherited from global climate models have been frequently reported to affect the prediction capability of regional climate models (Chen, 2021), and the signals of future changes between reginal and global climate models may be even opposite (Bartok et al., 2017). Moreover, the inconsistencies of spatial distributions further complicate the future changes in spatial heterogeneity of PBLH in China, while the corresponding governing mechanism remains unclear.

Considering the differences in GCMs performance, some studies apply a method to select models with better performances to improve the confidence of future projections. Based on the bias, Tung et al. (2020) selected five models with the higher skills in predicting Meiyu precipitation over Taiwan Province in China, and indicated a substantial increase of the Meiyu precipitation by the end of the century under RCP 8.5. Using a similar approach, Si et al. (2021) found that despite little progress in reducing the double Intertropical Convergence Zone bias in CMIP6 ensemble, top five models can be selected and largely reduced the bias. Based on CMIP6 shared socioeconomic pathways (SSPs) scenarios that combine social, economic and environmental development (Eyring et al., 2016; O'Neill et al., 2014; Stouffer et al., 2017), we analyze the inter-model differences in reproducing PBLH in summer and winter over China, and apply a model selection method to warrant the robustness of the future changes in PBLH as well as governing mechanisms.

This study is organized as follows. Section 2 presents the datasets and methods, followed by the evaluation of historical PBLH and related meteorological parameters influencing the PBLH in China from CMIP6 GCMs, as well as future projections and the associated mechanisms in Section 3. The conclusions and discussions are shown in Section 4.

2. Data and methods

2.1. Data selection

The reanalysis data used in this study is ERA5 from the European Centre for Medium-Range Weather Forecast (ECMWF) (https://cds.climate.copernicus.eu/#!/home, last access: 1 February 2022; (Hersbach et al., 2020)), including variables of PBLH, sensible heat flux (SHFLX), latent heat flux (LHFLX), precipitation, near surface wind speed, near surface relative humidity (RH) and total cloud cover. Monthly GCMs data are used from 13 CMIP6 models (https://esgf-node.llnl.gov/search/cmip6/, last access: 15 June 2022), with model information shown in Table 1. Four SSPs scenarios are selected, including SSP1–2.6, SSP2–4.5, SSP3–7.0 and SSP5–8.5 (O'Neill et al., 2016; Tebaldi et al., 2021). Air pollutant data is available at China National Environmental Monitoring Centre (http://www.pm25.in, last access: 1 February 2022).

2.2. Methods

The periods of 1995–2014 and 2080–2099 are considered as the historical and future periods, respectively. To facilitate the comparison, the CMIP6 model outputs and ERA5 reanalysis data are bilinearly interpolated to the same grid of 1° × 1° prior to the analysis. The confidence of future estimates can be characterized by signal-to-noise ratio (SNR) (Shi et al., 2018; Zhu et al., 2020).

$$\mathrm{SNR} = |x_e| / \sqrt{\frac{1}{n}\sum_{i=1}^{n}(x_i - x_e)^2}$$

where x_i represents the variable value simulated by a single model, x_e represents the variable value from multi-model ensemble mean, n is the number of models. The numerator and the denominator denote the signal and noise, respectively. SNR >1 represents a larger signal than noise, indicating considerable consistencies among the models and a high confidence of future projection.

The study area is shown in Fig. 1, and red rectangles outline the four regions focused in this study, including Beijing-Tianjin-Hebei region (BTH), the border area of Jiangsu, Anhui, Shandong and Henan (SWLY), Yangtze River Delta (YRD) and Pearl River Delta (PRD).

3. Results

3.1. Strong correlation between near surface air pollutants and PBLH

PBLH is a key factor affecting the vertical mixing and dilution of near surface pollutants (Seidel et al., 2010). By matching the ERA5 PBLH with near surface air pollutants, Fig. 2 shows the correlations between MDA8 O_3 and PBLH averaged during 9:00–16:00 LST in summer, and between daily mean $PM_{2.5}$ and PBLH in winter.

In summer, the correlations between PBLH and MDA8 O_3 are positive (Fig. 2a-d), possibly linked to the dilution of NO concentrations due to enhanced vertical mixing which weakens the NO titration effect (He et al., 2017), and strengthened downward transport of ozone from the free troposphere (Reddy et al., 2012; Sun et al., 2010). In addition, the increase of PBLH is usually accompanied by meteorological conditions that are conducive to ozone generation, such as high temperature and strong radiation (He et al., 2017; Liu and Wang, 2020). Therefore,

Table 1
List of 13 CMIP6 GCMs used in this study.

No.	Model	Institution/Country	Horizontal resolution(lon×lat)
1	CanESM5-CanOE	CCCMA/Canada	2.8° × 2.8°
2	CanESM5	CCCMA/Canada	2.8° × 2.8°
3	GFDL-ESM4	NOAA-GFDL/USA	1° × 1°
4	GISS-E2–1-G	NASA-GISS/USA	2.5° × 2°
5	GISS-E2–1-H	NASA-GISS/USA	2.5° × 2°
6	GISS-E2–2-G	NASA-GISS/USA	2.5° × 2°
7	INM-CM4–8	INM/Russia	2° × 1.5°
8	INM-CM5–0	INM/Russia	2° × 1.5°
9	MIROC-ES2L	MIROC/Japan	1.4° × 1.4°
10	NorESM2-LM	NCC/Norway	2.5° × 1.9°
11	NorESM2-MM	NCC/Norway	1.25° × 0.9°
12	TaiESM1	AS-RCEC/China	1.25° × 0.9°
13	UKESM1–0-LL	MOHC/UK	1.875° × 1.25°

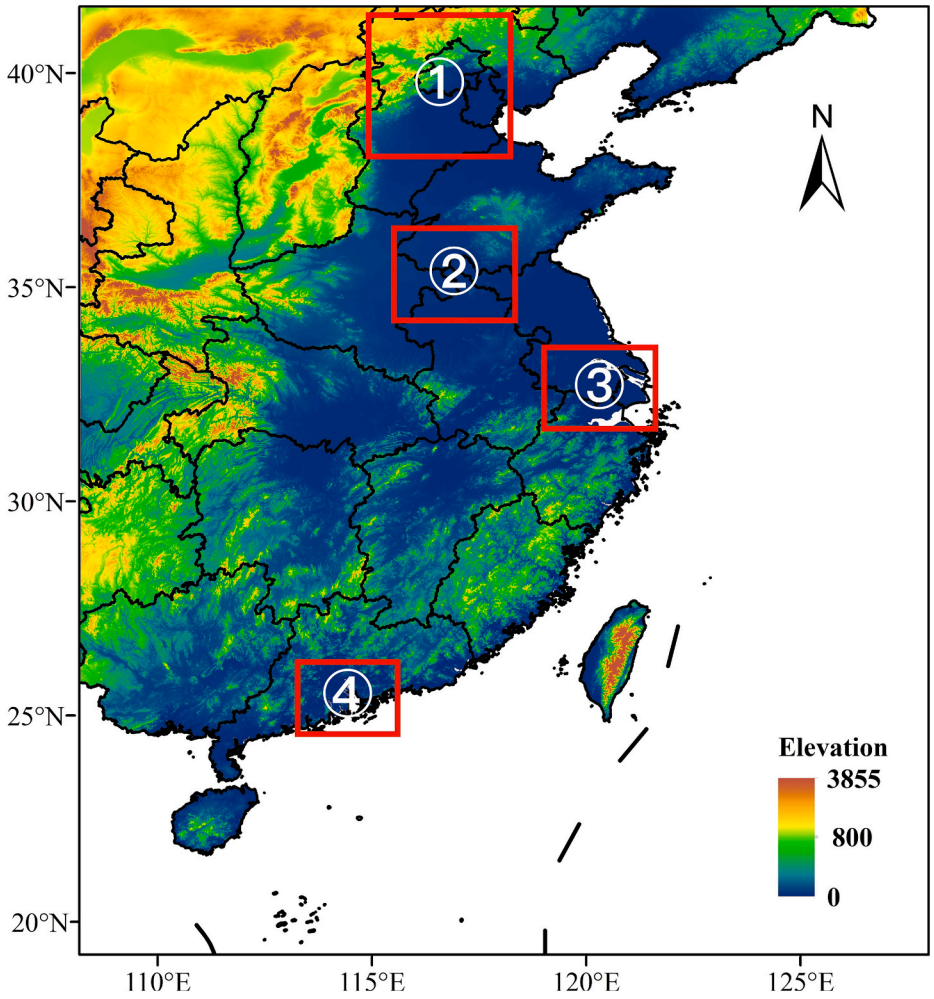

Fig. 1. The topography (unit: m) of the study area and the geographical locations of four regions (① BTH, ② SWLY, ③ YRD, ④ PRD) of the focus in this study.

various factors together lead to a positive correlation between PBLH and ozone. The largest positive correlation between PBLH and MDA8 O_3 appears over SWLY (Fig. 2b), indicating that ozone pollution in this region is more susceptible to PBLH.

In winter, the correlations between PBLH and $PM_{2.5}$ are negative (Fig. 2e-h). Lower PBLH is not conducive to the dispersion of air pollutants near the ground, resulting in higher $PM_{2.5}$ concentrations (Dong et al., 2017; Su et al., 2018). At the same time, in heavily polluted regions such as BTH and SWLY, high concentrations of $PM_{2.5}$ enhance the stability of the boundary layer through the aerosol radiation effect (Chen et al., 2023; Guan et al., 2020), thereby decreasing PBLH and further resulting in an increase in $PM_{2.5}$ concentrations (Petaja et al., 2016).

3.2. *CMIP6 model grouping based on evaluation of PBLH hindcast results*

The average seasonal PBLH from each CMIP6 model is compared with ERA5, and the mean biases of each model and CMIP6 multi-model ensemble (MME) in summer and winter are shown in Fig. 3a,b, respectively. Based on the biases, the sub-ensemble of five models with the smallest biases are considered as TOP-5 models. For the models with least performance capability, we select those with large positive biases without including the one (number 3) showing a large different (negative) sign of bias. Among the four selected regions, including BTH, SWLY, YRD and PRD, the mean biases in CMIP6 MME are 18% and 17%, respectively in summer and winter. The top ranking models better reproduce the PBLH, with the mean bias of 11% in summer (TOP-5; No. 1,2,4,5,6) and 5% in winter (TOP-5; No. 1,2,5,6,12) over the four regions. For the last ranking models (LAST-5), the mean PBLH biases over the four regions are 56% in summer and 55% in winter.

The box and whisker plots (Fig. 3c,d) show more intuitively that simulated PBLH by TOP-5 (green) is in general closer to that in ERA5 than that simulated by LAST-5 (red) and CMIP6 MME (orange). In summer, the mean PBLH over the four major regions is 506.51 m in ERA5, 495.81 m in TOP-5, 592.98 m and 784.67 m in CMIP6 MME and LAST-5, respectively. In winter, PBLH are generally lower than that in summer. The mean PBLH in CMIP6 MME and LAST-5 are 474.84 m and 628.41 m, respectively, exhibiting larger biases than TOP-5 (402.33 m) relative to ERA5 (406.77 m). In addition, the spatial distributions of PBLH biases in summer and winter from TOP-5, LAST-5 and CMIP6 MME are shown in Fig. S1, further illustrating the improvement of TOP-5 in delineating the spatial heterogeneity of PBLH.

To elucidate the possible reasons yielding the biases in PBLH, the associations between PBLH and a few key meteorological parameters are conducted. Sensible heat flux and latent heat flux are the most important energy sources for atmospheric circulation (Garratt, 1994), and the partitioning of energy between them dominates the development of PBLH (Zhou et al., 2021). Cloud cover is one of the factors leading to the long-term change of PBLH in China, and plays a key role in altering the energy distribution and balance of the surface (Yue et al., 2021). At the same time, PBLH is closely related to atmospheric stability, which in turn is driven by near surface temperature, wind speed and relative humidity (Huo et al., 2021; Zhang et al., 2013). Meanwhile, atmospheric stability affects the vertical movement of air masses and changes the ability of forming precipitation (Guo et al., 2022; Shin and Ha, 2005).

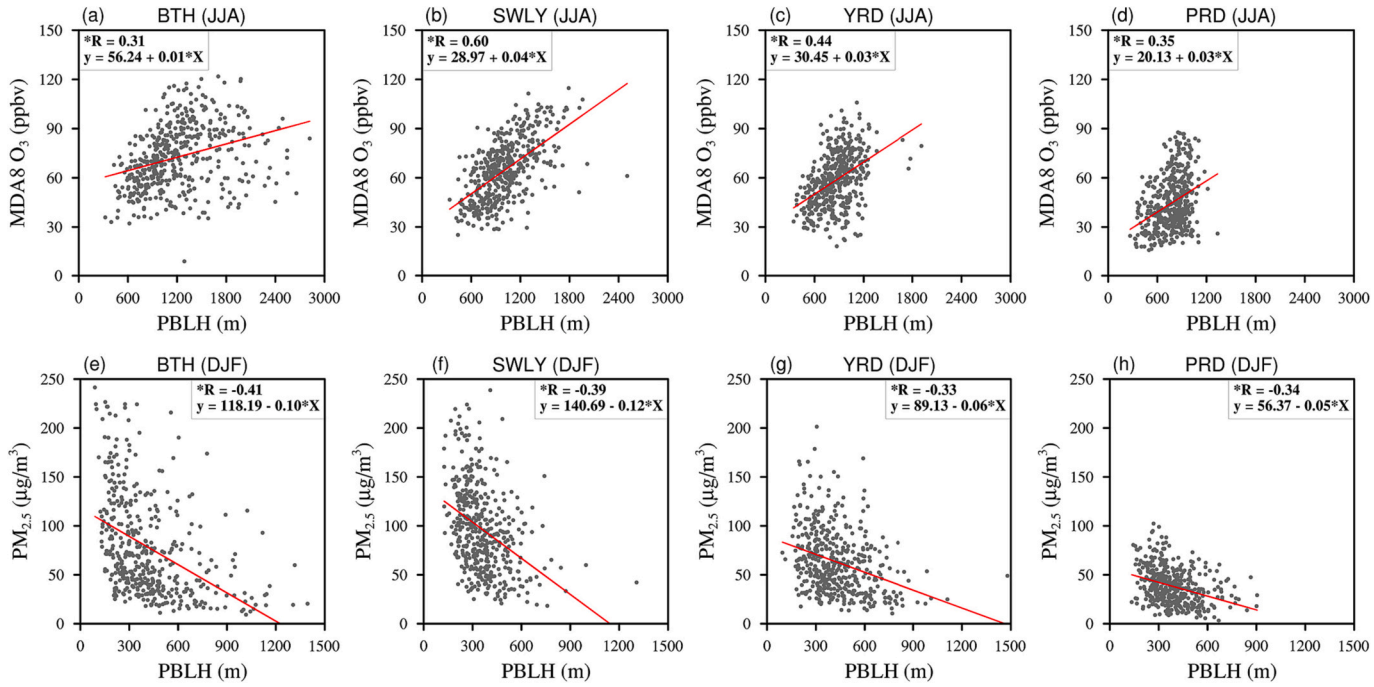

Fig. 2. The correlation between MDA8 O_3 and PBLH averaged over 9:00–16:00 LST in summer (a-d), and daily mean $PM_{2.5}$ and PBLH in winter (e-h) during 2015–2019 over four regions. The correlation coefficients (R) are labelled in each panel, with the asterisk on the top indicative of statistical significance ($p < 0.05$).

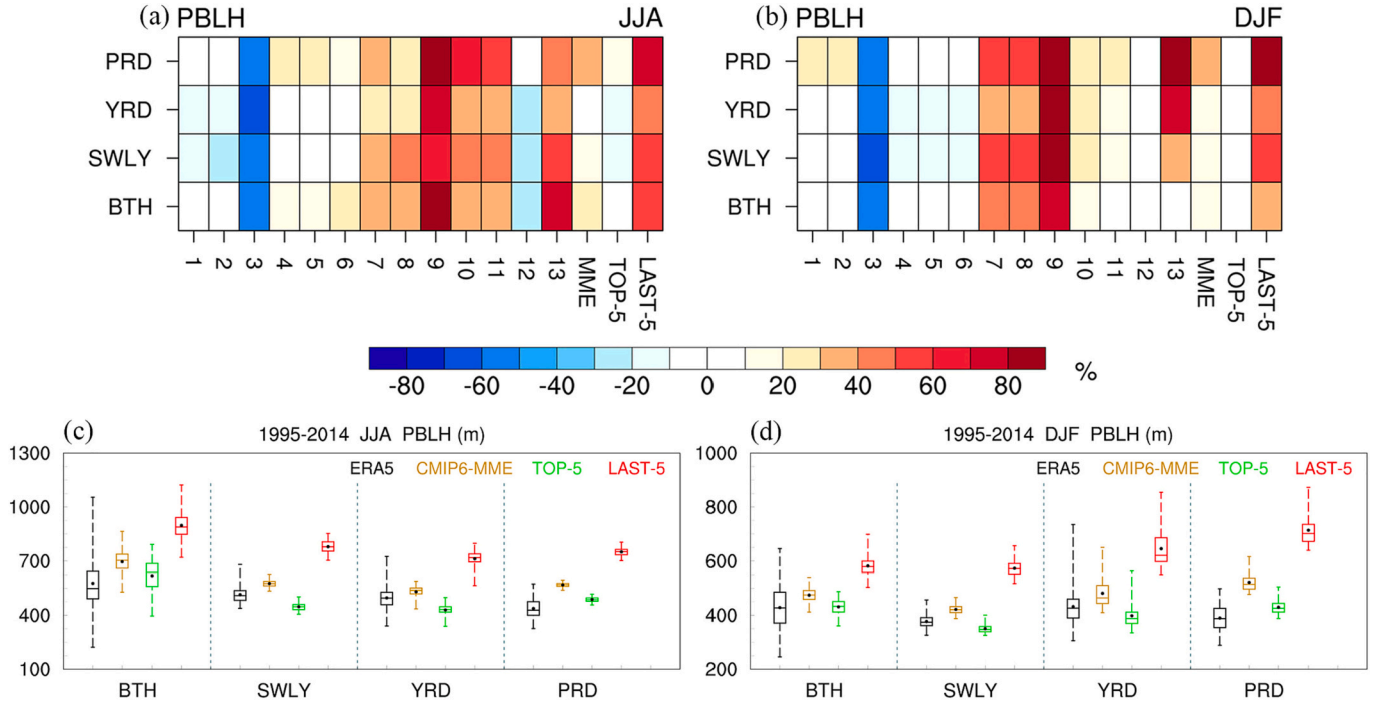

Fig. 3. Portrait diagrams of the PBLH relative errors (%) between CMIP6 models and the ERA5 reanalysis data during the period of 1995–2014 (a-b). The box and whisker plot displays the seasonal PBLH during the period of 1995–2014 over each region (c-d), with the minimum and maximum (line end points), 25th and 75th percentiles (boxes), medians (horizontal lines) and averages (black points). The top ranking models (TOP-5) and last ranking models (LAST-5) are identified from 13 models, with five models in each group. The numbers in the X Axis of Fig. 3a,b corresponds to the models listed in Table 1.

In order to determine the potential reasons that may lead to large deviations of PBLH in GCMs over China, the correlations between PBLH and the meteorological variables including SHFLX, LHFLX, precipitation, near surface wind speed, RH and total cloud cover among CMIP6 MME, TOP-5 and LAST-5 are shown in Fig. 4. Compared to CMIP6 MME and LAST-5 results, the relationships between PBLH and meteorological parameters exhibited in ERA5 are better reproduced by TOP-5 models in both summer and winter (Fig. 4b), with a correlation of 0.98, further indicating a strong confidence in applying TOP-5 model results to analyze future changes of PBLH in China. Moreover, among these meteorological factors, SHFLX and RH show the highest correlations of close to 1.0 and − 1.0, respectively, stressing stronger modulation

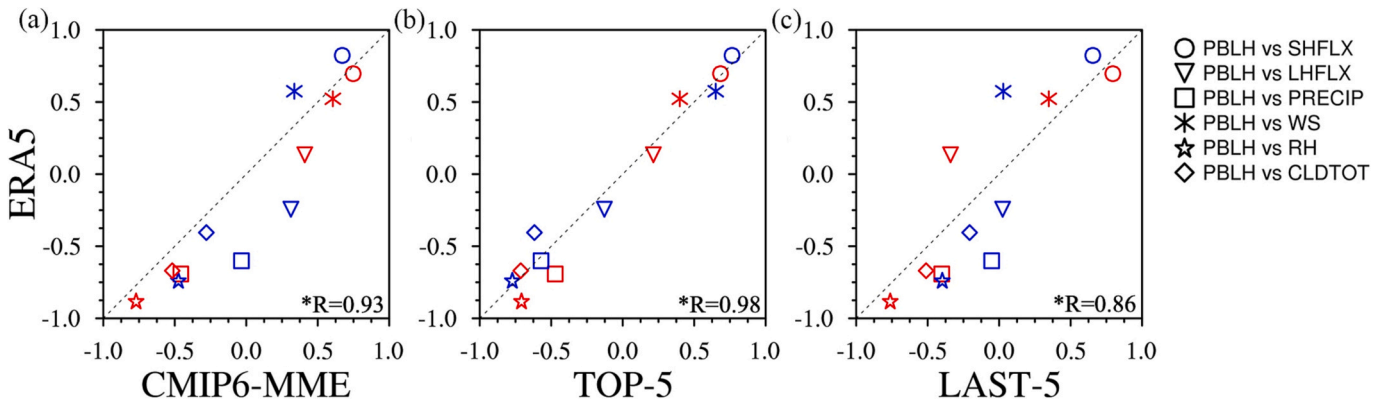

Fig. 4. Comparison of correlation coefficient between meteorological parameters and PBLH from ERA5 (Y Axis) reanalysis data and the results of models (X Axis), including CMIP6-MME (a), TOP-5 (b) and LAST-5 (c). The markers in red and blue represent summer and winter, respectively. The correlation coefficients (R) between ERA5 and models are given at the bottom right of each panel, with the asterisk on the top indicative of statistical significance ($p < 0.05$). (For interpretation of the references to color in this figure legend, the reader is referred to the web version of this article.)

effects relative to other parameters. Considering the strongly positive correlation between PBLH and SHFLX, biases in PBLH is to a large degree associated with the deficiencies in simulating SHFLX in CMIP6 models, which are in part associated with biases of downward surface solar radiation (Betts and Dias, 2010; Yue et al., 2021), and higher-resolution Earth sysmte models are desirable in reproducing the downward surface solar radiation (Kou et al., 2023).

3.3. Divergence of future PBLH in CMIP6 models

Fig. 5 shows the spatial distributions of projected summer changes in PBLH from CMIP6 MME, TOP-5 and LAST-5 under SSP1–2.6, SSP2–4.5, SSP3–7.0 and SSP5–8.5 scenarios at the end of the 21st century (2080–2099). For TOP-5 models, PBLH is projected to change featured by a dipole in the northern and southern China (Fig. 5b,e,h,k). Specifically, PBLH tends to decrease substantially by the end of the century in North China, with the largest magnitude in SSP3–7.0, whereas the changes of PBLH over central and southern China are projected to increase, with the largest increases under the fossil fuel intensive scenario of SSP5–8.5. This dipole feature is missed by LAST-5 and CMIP6 MME to a large extent, with a low model agreement and SNR values less than one, indicative of a much-weakened confidence in future projections compared to the signal exhibited by TOP-5 models. The dipole pattern of PBLH changes in China is, however, displayed in a previous study which applied dynamical downscaling and simulations with a regional model under RCP 4.5 and RCP 8.5 scenarios (Dou et al., 2021), strengthening the confidence of the spatial heterogeneity of PBLH in responding to a warming climate.

Among the meteorological parameters affecting the PBLH, SHFLX and RH have the highest correlations with PBLH during the historical period (Fig. 4). Thus, the projected changes of SHFLX and PBLH from the TOP-5 models show similar spatial dipole patterns over China (Fig. 6a-d vs. Fig. 5b,e,h,k), while the changes of near surface RH exhibit an opposite and consistent spatial dipole patterns (Fig. 6e-h). It suggests that future changes of PBLH in CMIP6 models are closely related to SHFLX and RH in summer, which not only holds for TOP-5 models (Fig. 6), but also applies to CMIP6 MME (Fig. S2) and LAST-5 models (Fig. S3), although the dipole feature emerged in TOP5 may have partly missed in CMIP6 MME and LAST-5. In terms of the larger reduction of PBLH in SSP3–7.0 compared to the other scenarios (Fig. 5h vs. Fig. 5b,e,k), the changes of SHFLX and RH do exhibit in stronger magnitudes in SSP3–7.0 correspondingly (Fig. 6c,g vs. Fig. 6a,b,d,e,f,h). Moreover, it is possibly linked to the emission increase under SSP3–7.0 in the future (32% in VOCs and 20% in NO_x; Fig. 2 in Zeng et al. (2022)), whereas the emissions in other scenarios such as SSP1–2.6, SSP2–4.5 and SSP5–8.5 are projected to decrease, and the aerosol radiative effect in SSP3–7.0 on PBLH tends to become stronger, triggering a larger decrease of PBLH.

The dipole feature of PBLH decrease in northern China and increase in southern China in the future is to a certain extent appears in winter (Fig. S4) particularly of the results of TOP-5 models. However, instead of sign differences of PBLH in summer between northern and southern China, the dipole is characterized by a stronger increase of PBLH in southern China and weaker increase in northern China (Fig. S4b, e, h, k) in winter, though consistencies among scenarios are relatively loose. The primary driving mechanism remains to lie in the modulation of SHFLX and RH in terms of the consistencies in the spatial distributions (Figs. S5b,e,h,k, S6b,e,h,k vs. Fig. S4b,e,h,k). The characteristics are largely missed in the results of CMIP6-MME and LAST-5 models (Figs. S4, S5, S6).

3.4. Discussion of potential mechanisms and implications

In order to further examine the governing mechanisms of SHFLX and RH on future changes of PBLH in the selected regions, relationships between PBLH and these two variables are shown in Fig. 7. In BTH, for TOP-5, SHFLX is projected to experience a decrease by 0.35 W/m^2, 4.43 W/m^2 and 0.67 W/m^2 in SSP2–4.5, SSP3–7.0 and SSP5–8.5, and the corresponding decreases of PBLH are 11.92 m, 42.90 m and 13.84 m under these scenarios, respectively. In contrast, the changes in BTH from LAST-5 and CMIP6 MME are mostly positive (Fig. 7a). For the regions of SWLY, YRD and PRD, the mean increases of PBLH in TOP-5 under the four scenarios are 60.21 m, 35.65 m and 29.76 m, respectively, whereas the corresponding mean increases of SHFLX are 5.42 W/m^2, 1.17 W/m^2 and 0.91 W/m^2, and the increases of PBLH and SHFLX are consistent with CMIP6 MME (Fig. 7b,c,d). At the same time, the projected changes of near surface RH are negatively correlated with PBLH in both summer and winter (Figs. 7 and S7). The increase of RH leads to enhanced latent heat flux, which inhibits the convective process in the boundary layer, resulting in a decrease in PBLH, while a decrease of RH favors moisture diffusion and convective transport and tends to trigger higher PBLH (Liu et al., 2018; Miao et al., 2019; Zhou et al., 2021).

Similar results are also observed in winter (Fig. S7). However, the correlation coefficients between changes in SHFLX and PBLH are much weaker in the northern China, which is likely due to the weaker solar radiation and surface heat flux in winter (Schneider and Eixmann, 2002), as well as the diminished effect of land-atmosphere interaction in the boreal winter (Dirmeyer, 2003).

Land surface models (LSMs) play a crucial role in the energy partitioning in climate models (Berg et al., 2016; Irannejad et al., 2003; Merrifield and Xie, 2016; Ukkola et al., 2018). Previous studies have shown that one of the main sources of uncertainties in global land surface modeling is the meteorological data used to drive LSMs (Jung et al.,

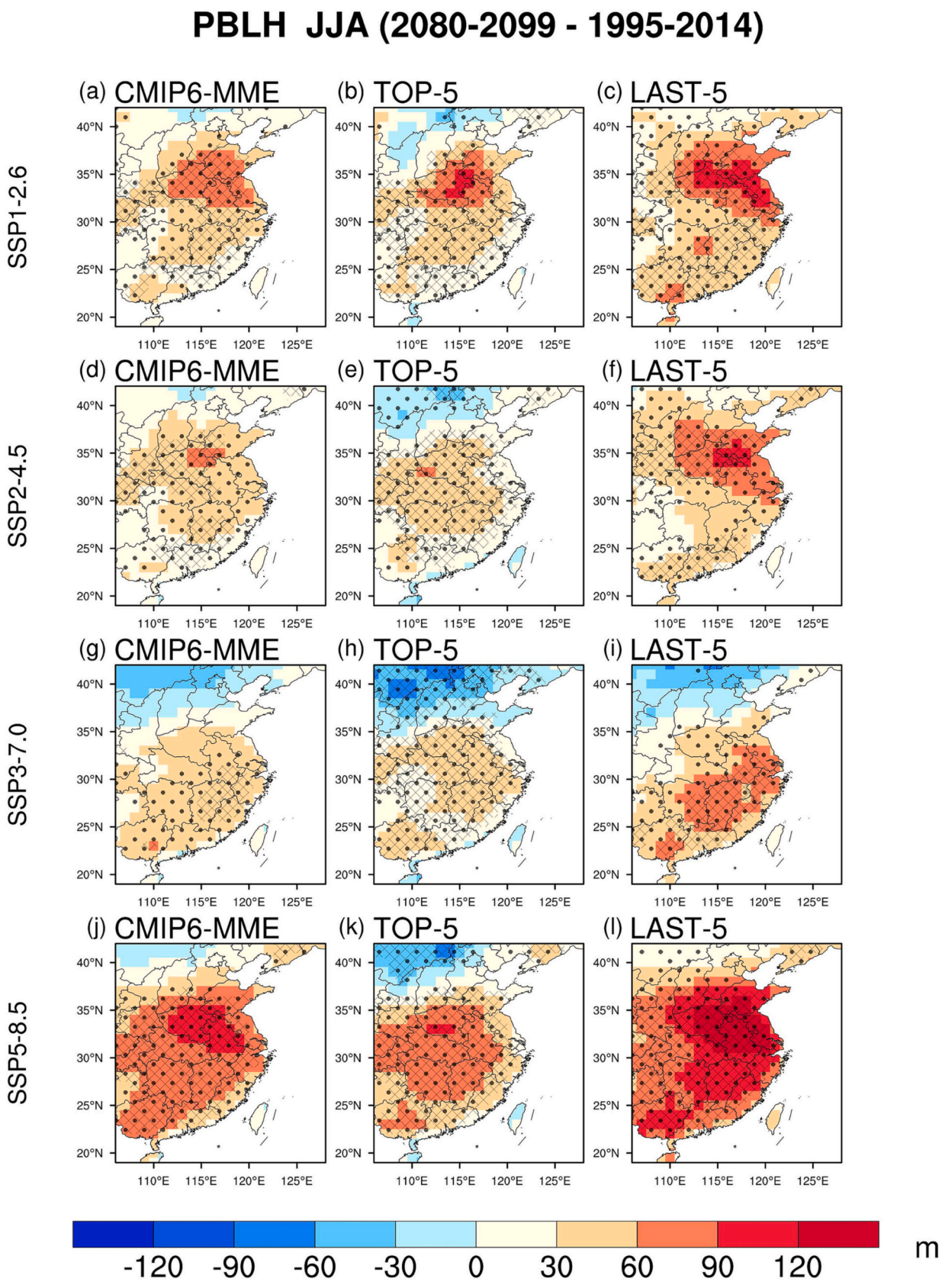

Fig. 5. Projected ensemble mean (left), TOP-5 (middle) and LAST-5 (right) changes of PBLH (m) in summer during 2080–2099 under SSP1–2.6 (a-c), SSP2–4.5 (d-f), SSP3–7.0 (g-i) and SSP5–8.5 (j-l), relative to 1995–2014. The black dots indicate where at least four-fifths of the models agree on the sign of change. The areas where SNR $>$ 1 are hatched.

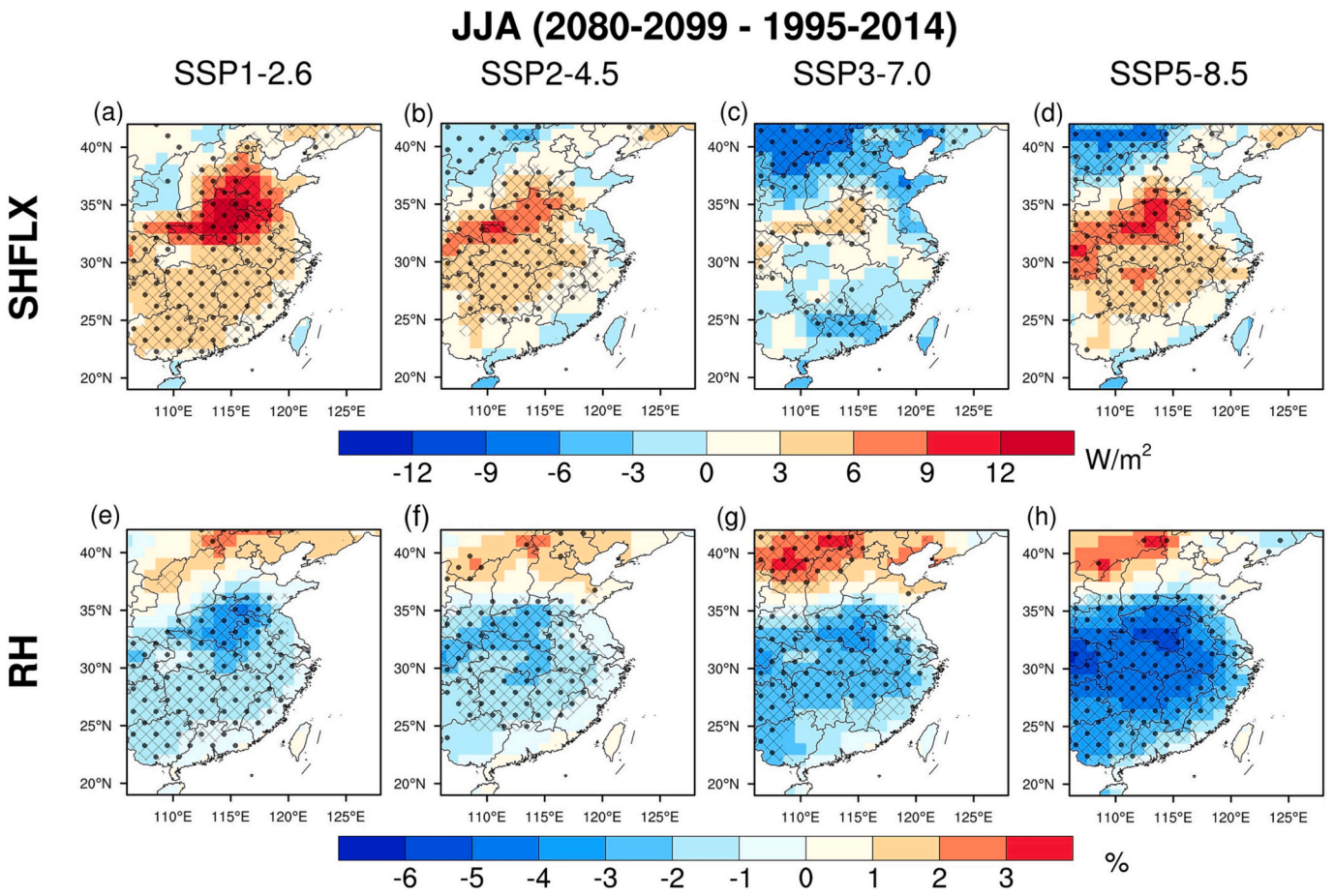

Fig. 6. Projected TOP-5 changes of SHFLX (top) and RH (bottom) in summer during 2080–2099 under SSP1–2.6 (a, e), SSP2–4.5 (b, f), SSP3–7.0 (c, g) and SSP5–8.5 (d, h), relative to 1995–2014. The black dots indicate where at least four-fifths of the models agree on the sign of change. The areas where SNR > 1 are indicated by grid patterns.

2007; Shrestha et al., 2020; Wang et al., 2016), and the behavior of LSMs is closely associated with the accuracy of meteorological variables. For instance, Fan et al. (2020) found that the overestimation of SHFLX and LHFLX on land in CMIP6 models was largely attributed to overestimates of surface humidity and underestimates of near surface air temperature. These biases of meteorological parameters (Fig. S8) may be attributed to errors of CMIP6 model inputs, inappropriate model parameterizations and land-atmosphere coupling (Dirmeyer et al., 2013; Hourdin et al., 2017; Li et al., 2021; McNeall et al., 2016). In addition to the biases resulting from meteorology, inaccuracy of land model physics and land cover also contribute to the biases in LSMs (Li et al., 2018; Wartenburger et al., 2018). Furthermore, the role of model resolution in improving the performance of LSMs has been highlighted. Higher horizontal and vertical resolutions have been found to better capture the spatial and temporal variability of surface fluxes over complex terrain in tropical regions (Zhou et al., 2020), and the distribution of SHFLX and LHFLX can be substantially improved based on high-resolution (0.25°) Earth system model simulations compared to CMIP5 (Gao et al., 2023). Given the interactions between land and atmosphere in current CMIP6 LSM models are not well represented, improvement of LSMs are vital to obtain a well reproduced PBLH.

4. Conclusions

This study thoroughly investigates the capability of CMIP6 multi-model ensemble in reproducing the historical PBLH, and identifies two groups of models showing small and large discrepancies in PBLH simulations over China, respectively. We further determine a group of models with better performance, and indicate that the ability in simulating a few key meteorological variables may determine the performance of PBLH. Then, we discuss the consistencies in future projections of PBLH in China and the associated mechanism. In both summer and winter, TOP-5 reasonably captures the spatial distributions of PBLH. The results of TOP-5 show a clear dipole feature of future changes in PBLH in both summer and winter. In summer, PBLH decreases in northern China and increases in southern China, while in winter, the spatial dipole is characterized by a stronger increase of PBLH in southern China and a weaker increase in northern China. The change of PBLH is largely modulated by changes in SHFLX and RH, indicating the vital role of governance in the land-atmosphere interactions on PBLH.

The influence of PBLH on major air pollutants including ozone and $PM_{2.5}$ behaves differently. For instance, low PBLH favors the accumulation of $PM_{2.5}$, and the boundary layer-aerosol interactions may further induce a shallower PBLH and exacerbate surface $PM_{2.5}$ concentrations (Ding et al., 2016; Petaja et al., 2016; Su et al., 2020; Wang et al., 2020). In contrast, the effect of PBLH on near-surface ozone is distinctive. Deep PBLH promotes photochemical reactions of ozone precursors, resulting in increased ozone concentrations (He et al., 2017; Liu and Wang, 2020; Ma et al., 2021). By the end of the 21st century, the findings of the changes of PBLH in this study indicate that the future decrease of PBLH in summer over northern China may favor a concomitant decrease of ozone concentrations, while in southern China the aggravated effect may be reinforced resulting from the increase of PBLH. In winter, PBLH is projected to increase in a large degree over southern China, which is conducive to the dispersion and decrease of $PM_{2.5}$ concentrations. The exact effects of PBLH on ozone and $PM_{2.5}$ need further investigation in

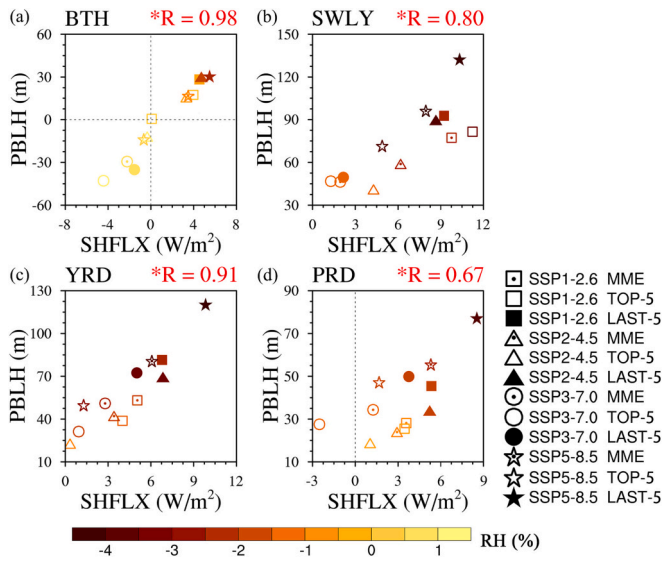

Fig. 7. The inter-model relationships between projected changes of PBLH (m) and SHFLX (W/m^2) in each model group in summer during 2080–2099 under SSP1–2.6 (square), SSP2–4.5 (triangle), SSP3–7.0 (circle) and SSP5–8.5 (pentagram) over BTH (a), SWLY (b), YRD (c) and PRD (d), relative to 1995–2014. The correlation coefficients (R) are given at the top right of each panel, with the asterisk on the top indicative of statistical significance ($p < 0.05$). The color-shaded patterns indicate projected changes of RH (%) in each model group.

the future. Our analysis provides useful information and high confidence of the future projections of PBLH, which is helpful to support future air quality studies in China. Considering high-resolution earth system model may exhibit an enhanced capability in simulating surface energy such as sensible heat flux and latent heat flux, a higher-resolution model development is one of the key directions in improving the simulations of PBLH as well as air pollutants (Zhang et al., 2023).

CRediT authorship contribution statement

Junlei Meng: Formal analysis, Writing – original draft. **Yang Gao:** Conceptualization, Methodology, Writing – review & editing. **Yuhang Wang:** Conceptualization, Writing – review & editing. **Lifang Sheng:** Writing – review & editing. **Shaoqing Zhang:** Writing – review & editing.

Declaration of Competing Interest

The authors declare that they have no known competing financial interests or personal relationships that could have appeared to influence the work reported in this paper.

Data availability

Data will be made available on request.

Acknowledgments

This research was supported by the National Key Research and Development Program of China (2022YFE0106400). Y.W. was supported by the National Science Foundation Atmospheric Chemistry Program. The analysis was conducted on the Center for High Performance Computing and System Simulation, National Laboratory for Marine Science and Technology (Qingdao).

Appendix A. Supplementary data

Supplementary data to this article can be found online at https://doi.org/10.1016/j.atmosres.2023.106975.

References

Bartok, B., et al., 2017. Projected changes in surface solar radiation in CMIP5 global climate models and in EURO-CORDEX regional climate models for Europe. Clim. Dyn. 49, 2665–2683.
Berg, A., et al., 2016. Land-atmosphere feedbacks amplify aridity increase over land under global warming. Nat. Clim. Chang. 6, 869–+.
Betts, A.K., Dias, M., 2010. Progress in understanding land-surface-atmosphere coupling from LBA research. J. Adv. Model. Earth Syst. 2, 8.
Chen, L., 2021. Uncertainties in solar radiation assessment in the United States using climate models. Clim. Dyn. 56, 665–678.
Chen, L., et al., 2023. Striking impacts of biomass burning on PM2.5 concentrations in Northeast China through the emission inventory improvement. Environ. Pollut. 318, 120835.
Dang, R.J., Qiu, X.B., Yang, Y., Zhang, S.W., 2022. Observation system simulation experiments (OSSEs) for assimilation of the planetary boundary-layer height (PBLH) using the EnSRF technique. Q. J. R. Meteorol. Soc. 148, 1184–1207.
Davy, R., 2018. The climatology of the atmospheric boundary layer in contemporary global climate models. J. Clim. 31, 9151–9173.
Davy, R., Esau, I., 2016. Differences in the efficacy of climate forcings explained by variations in atmospheric boundary layer depth. Nat. Commun. 7, 11690.
Ding, A.J., et al., 2016. Enhanced haze pollution by black carbon in megacities in China. Geophys. Res. Lett. 43, 2873–2879.
Dirmeyer, P.A., 2003. The role of the land surface background state in climate predictability. J. Hydrometeorol. 4, 599–610.
Dirmeyer, P.A., Jin, Y., Singh, B., Yan, X.Q., 2013. Trends in Land-Atmosphere Interactions from CMIP5 Simulations. J. Hydrometeorol. 14, 829–849.
Dong, Z.P., Li, Z.Q., Yu, X., Cribb, M., Li, X.M., Dai, J., 2017. Opposite long-term trends in aerosols between low and high altitudes: a testimony to the aerosol-PBL feedback. Atmos. Chem. Phys. 17, 7997–8009.
Dou, C.R., Ji, Z.M., Xiao, Y.K., Hu, Z.Y., Zhu, X., Dong, W.J., 2021. Projection of air pollution in Northern China in the two RCPs scenarios. Remote Sens. 13, 3064.
Eyring, V., Bony, S., Meehl, G.A., Senior, C.A., Stevens, B., Stouffer, R.J., Taylor, K.E., 2016. Overview of the Coupled Model Intercomparison Project Phase 6 (CMIP6) experimental design and organization. Geosci. Model Dev. 9, 1937–1958.
Fan, X.W., Duan, Q.Y., Shen, C.W., Wu, Y., Xing, C., 2020. Global surface air temperatures in CMIP6: historical performance and future changes. Environ. Res. Lett. 15, 104056.
Gao, D., Xie, M., Chen, X., Wang, T.J., Zhan, C.C., Ren, J.Y., Liu, Q., 2019. Modeling the effects of climate change on surface ozone during summer in the Yangtze River Delta region, China. Int. J. Environ. Res. Public Health 16, 1528.
Gao, Y., et al., 2023. More frequent and persistent heat waves due to increased temperature skewness projected by a high-resolution Earth System Model. Geophys. Res. Lett. in review.
Garratt, J.R., 1994. The atmospheric boundary layer – review. Earth Sci. Rev. 37, 89–134.
Guan, S.H., Wong, D.C., Gao, Y., Zhang, T.Q., Pouliot, G., 2020. Impact of wildfire on particulate matter in the southeastern United States in November 2016. Sci. Total Environ. 724, 138354.
Guo, Y.L., Zhang, W.Y., Mao, L.X., Wang, K.Q., 2022. Characteristics and relationships between daily maximum boundary layer height and precipitation in the arid and semi-arid regions of East Asia. WEATHER 77, 181–188.
He, J.J., et al., 2017. Air pollution characteristics and their relation to meteorological conditions during 2014-2015 in major Chinese cities. Environ. Pollut. 223, 484–496.
Hersbach, H., et al., 2020. The ERA5 global reanalysis. Q. J. R. Meteorol. Soc. 146, 1999–2049.
Hourdin, F., et al., 2017. The art and science of climate model tuning. Bull. Am. Meteorol. Soc. 98, 589–602.
Huo, Y.F., et al., 2021. Trends of planetary boundary layer height over urban cities of China from 1980-2018. Front. Environ. Sci. 9, 744255.
Irannejad, P., Henderson-Sellers, A., Sharmeen, S., 2003. Importance of land-surface parameterization for latent heat simulation in global atmospheric models. Geophys. Res. Lett. 30, 1904.
Jung, M., et al., 2007. Uncertainties of modeling gross primary productivity over Europe: a systematic study on the effects of using different drivers and terrestrial biosphere models. Glob. Biogeochem. Cycles 21, GB4021.
Kou, W.B., et al., 2023. High downward surface solar radiation conducive to ozone pollution more frequent under global warming. Sci. Bull. 68, 388–392.
Li, Z.Q., et al., 2017. Aerosol and boundary-layer interactions and impact on air quality. Natl. Sci. Rev. 4, 810–833.
Li, J.D., Duan, Q.Y., Wang, Y.P., Gong, W., Gan, Y.J., Wang, C., 2018. Parameter optimization for carbon and water fluxes in two global land surface models based on surrogate modelling. Int. J. Climatol. 38, E1016–E1031.
Li, J.D., Miao, C.Y., Wei, W., Zhang, G., Hua, L.J., Chen, Y.L., Wang, X.X., 2021. Evaluation of CMIP6 Global Climate Models for Simulating Land surface energy and water fluxes during 1979-2014. J. Adv. Model. Earth Syst. 13 e2021MS002515.
Liu, Y.M., Wang, T., 2020. Worsening urban ozone pollution in China from 2013 to 2017-Part 1: the complex and varying roles of meteorology. Atmos. Chem. Phys. 20, 6305–6321.

Liu, Q., et al., 2018. New positive feedback mechanism between boundary layer meteorology and secondary aerosol formation during severe haze events. Sci. Rep. 8, 6095.
Ma, X.D., Huang, J.P., Zhao, T.L., Liu, C., Zhao, K.H., Xing, J., Xiao, W., 2021. Rapid increase in summer surface ozone over the North China Plain during 2013-2019: a side effect of particulate matter reduction control? Atmos. Chem. Phys. 21, 1–16.
McNeall, D., Williams, J., Booth, B., Betts, R., Challenor, P., Wiltshire, A., Sexton, D., 2016. The impact of structural error on parameter constraint in a climate model. Earth Syst. Dyn. 7, 917–935.
Merrifield, A.L., Xie, S.P., 2016. Summer US surface air temperature variability: controlling factors and AMIP simulation biases. J. Clim. 29, 5123–5139.
Miao, Y.C., et al., 2019. Interaction between planetary boundary layer and PM2.5 pollution in megacities in China: a review. Curr. Pollut. Rep. 5, 261–271.
O'Neill, B.C., et al., 2014. A new scenario framework for climate change research: the concept of shared socioeconomic pathways. Clim. Chang. 122, 387–400.
O'Neill, B.C., et al., 2016. The Scenario Model Intercomparison Project (ScenarioMIP) for CMIP6. Geosci. Model Dev. 9, 3461–3482.
Petaja, T., et al., 2016. Enhanced air pollution via aerosol-boundary layer feedback in China. Sci. Rep. 6, 18998.
Reddy, K.K., Naja, M., Ojha, N., Mahesh, P., Lal, S., 2012. Influences of the boundary layer evolution on surface ozone variations at a tropical rural site in India. J. Earth Syst. Sci. 121, 911–922.
Schneider, J., Eixmann, R., 2002. Three years of routine Raman lidar measurements of tropospheric aerosols: backscattering, extinction, and residual layer height. Atmos. Chem. Phys. 2, 313–323.
Seidel, D.J., Ao, C.O., Li, K., 2010. Estimating climatological planetary boundary layer heights from radiosonde observations: comparison of methods and uncertainty analysis. J. Geophys. Res.-Atmos. 115, D16113.
Shi, C., Jiang, Z.H., Chen, W.L., Li, L., 2018. Changes in temperature extremes over China under 1.5 degrees C and 2 degrees C global warming targets. Adv. Clim. Chang. Res. 9, 120–129.
Shin, S., Ha, K.-J., 2005. Impact of improvement of Variable Depth PBL parameterization on a GCM. Asia-Pac. J. Atmos. Sci. 41, 717–732.
Shrestha, A., Nair, A.S., Indu, J., 2020. Role of precipitation forcing on the uncertainty of land surface model simulated soil moisture estimates. J. Hydrol. 580, 124264.
Si, W., Liu, H.L., Zhang, X.X., Zhang, M.H., 2021. Double intertropical convergence zones in coupled ocean-atmosphere models: progress in CMIP6. Geophys. Res. Lett. 48 e2021GL094779.
Stocker, B.D., et al., 2013. Multiple greenhouse-gas feedbacks from the land biosphere under future climate change scenarios. Nat. Clim. Chang. 3, 666–672.
Stouffer, R.J., Eyring, V., Meehl, G.A., Bony, S., Senior, C., Stevens, B., Taylor, K.E., 2017. CMIP5 scientific gaps and recommendations for CMIP6. Bull. Am. Meteorol. Soc. 98, 95–+.
Stull, R.B., 2006. The Atmospheric Boundary Layer, pp. 375–417.
Su, T.N., Li, Z.Q., Kahn, R., 2018. Relationships between the planetary boundary layer height and surface pollutants derived from lidar observations over China: regional pattern and influencing factors. Atmos. Chem. Phys. 18, 15921–15935.
Su, T.N., Li, Z.Q., Zheng, Y.T., Luan, Q.Z., Guo, J.P., 2020. Abnormally shallow boundary layer associated with severe air pollution during the COVID-19 lockdown in China. Geophys. Res. Lett. 47 e2020GL090041.
Sun, Y., Wang, Y.S., Zhang, C.C., 2010. Vertical observations and analysis of PM2.5, O-3, and NO (x) at Beijing and Tianjin from towers during summer and Autumn 2006. Adv. Atmos. Sci. 27, 123–136.
Tebaldi, C., et al., 2021. Climate model projections from the Scenario Model Intercomparison Project (ScenarioMIP) of CMIP6. Earth Syst. Dyn. 12, 253–293.
Tung, Y.S., Wang, S.Y.S., Chu, J.L., Wu, C.H., Chen, Y.M., Cheng, C.T., Lin, L.Y., 2020. Projected increase of the East Asian summer monsoon (Meiyu) in Taiwan by climate models with variable performance. Meteorol. Appl. 27, e1886.
Ukkola, A.M., Pitman, A.J., Donat, M.G., De Kauwe, M.G., Angelil, O., 2018. Evaluating the contribution of land-atmosphere coupling to heat extremes in CMIP5 models. Geophys. Res. Lett. 45, 9003–9012.
Vignon, E., Hourdin, F., Genthon, C., van de Wiel, B.J.H., Gallee, H., Madeleine, J.B., Beaumet, J., 2018. Modeling the dynamics of the atmospheric boundary layer over the Antarctic Plateau with a general circulation model. J. Adv. Model. Earth Syst. 10, 98–125.
von Engeln, A., Teixeira, J., 2013. A planetary boundary layer height climatology derived from ECMWF reanalysis data. J. Clim. 26, 6575–6590.
Wang, A.H., Zeng, X.B., Guo, D.L., 2016. Estimates of global surface hydrology and heat fluxes from the Community Land Model (CLM4.5) with four atmospheric forcing datasets. J. Hydrometeorol. 17, 2493–2510.
Wang, Y.H., et al., 2020. Rapid formation of intense haze episodes via aerosol-boundary layer feedback in Beijing. Atmos. Chem. Phys. 20, 45–53.
Wartenburger, R., et al., 2018. Evapotranspiration simulations in ISIMIP2a-Evaluation of spatio-temporal characteristics with a comprehensive ensemble of independent datasets. Environ. Res. Lett. 13, 075001.
Yue, M., Wang, M.H., Guo, J.P., Zhang, H.P., Dong, X.Y., Liu, Y.W., 2021. Long-Term trend comparison of planetary boundary layer height in observations and CMIP6 Models over China. J. Clim. 34, 8237–8256.
Zeng, X.R., Gao, Y., Wang, Y.H., Ma, M.C., Zhang, J.X., Sheng, L.F., 2022. Characterizing the distinct modulation of future emissions on summer ozone concentrations between urban and rural areas over China. Sci. Total Environ. 820, 153324.
Zhang, Y.H., Seidel, D.J., Zhang, S.D., 2013. Trends in planetary boundary layer height over Europe. J. Clim. 26, 10071–10076.
Zhang, S.Q., et al., 2023. Toward Earth system modeling with resolved clouds and ocean submesoscales on heterogeneous many-core HPCs. Natl. Sci. Rev. 10, nwad069.
Zhou, X., Ray, P., Barrett, B.S., Hsu, P.C., 2020. Understanding the bias in surface latent and sensible heat fluxes in contemporary AGCMs over tropical oceans. Clim. Dyn. 55, 2957–2978.
Zhou, L.M., Tian, Y.H., Wei, N., Ho, S.P., Li, J., 2021. Rising planetary boundary layer height over the Sahara Desert and Arabian Peninsula in a warming climate. J. Clim. 34, 4043–4068.
Zhu, S.P., Ge, F., Fan, Y., Zhang, L., Sielmann, F., Fraedrich, K., Zhi, X.F., 2020. Conspicuous temperature extremes over Southeast Asia: seasonal variations under 1.5 degrees C and 2 degrees C global warming. Clim. Chang. 160, 343–360.